3D COMPUTATION OF SINGLE-EXPANSION-RAMP AND SCRAMJET NOZZLES

H. T. Lai
Sverdrup Technology, Inc.
NASA Lewis Research Center Group
Cleveland, Ohio 44135

ABSTRACT

Description of the computations for three-dimensional nonaxisymmetric nozzles and analysis of the flowfields are presented in this paper. Two different types of nozzles are investigated for compressible flows at high Reynolds numbers. These are the single-expansion-ramp and scramjet nozzles. The computation for the single-expansion-ramp nozzle focuses on the condition of low pressure ratio, which requires the simulation for turbulent flow that is not needed at high pressure ratios. The flowfield contains the external quiescent air, and the internal regions of subsonic and low supersonic flows. The second type is the scramjet nozzle, which typically has a very large area ratio and is designed to operate at high speeds and pressure ratios. The freestream external flow has a Mach number of 6, and the internal flow leaving the combustion chamber is at a Mach number of 1.62. The flowfield is mostly supersonic except in the viscous region near walls. The computed results from both cases are compared with experimental data for the surface pressure distributions.

INTRODUCTION

Numerical flowfields in three dimensions are presented and analyzed for the single-expansion-ramp and scramjet nozzles. These nozzles are nonaxisymmetric because of the geometry of the upper and lower nozzle walls, in which one of the walls is longer than the other. The diverging exit provides the flow an additional external free expansion over the long surface, i.e, an expansion ramp, and allows the exhaust plume behind the nozzle to deflect away from the nozzle axis according to the pressure difference between the internal and ambient flows. The resulting flow structure requires the numerical computation to account for the interaction between the internal flow and the external freestream. This mixing interaction occurs through a free shear layer, which is encountered frequently in the exhaust flows. The shear layers emanating from the short surfaces, i.e., a cowl or a splitter plate, and the nozzle sidewalls, are especially significant. Along with these mixing layers at the edges, expansion fans, compression or shock waves, which are determined by the deflection angles of the shear layers, also emerge and could have large effects on the

overall nozzle flowfield. The simulation described here is formulated to include in three dimensions a computational domain that contains the external freestream surrounding the nozzle, in addition to the typical internal converging/diverging section. Consequently, the procedure allows various features of flow interaction to develop. The PARC computer code [1] is employed to model the viscous flowfields for two similar nonaxisymmetric nozzles at high Reynolds numbers. The flowfield for the single-expansion-ramp nozzle consists of regions of internal subsonic/supersonic expansions and an external plume exhausting into a quiescent ambient environment. A substantial flow portion in the quiescent air has very low velocities. This type of nozzle has been investigated experimentally by Re and Leavitt [2] to determine the effects of various geometrical parameters and pressure ratios on nozzle static performance. On the other hand, the scramjet nozzle having large exit-to-throat area ratio is designed to operate at very high speeds and pressure ratios. The flow leaving the combustion chamber has a Mach number of 1.62, whereas the external freestream Mach number is 6. The flowfield is predominantly supersonic at high Mach numbers, except in thin subsonic boundary layers adjacent to the nozzle walls. Experimental work on this scramjet nozzle was performed by Cubbage and Monta [3] to study the flowfield behavior at different geometry and flow conditions. Although air and other simulant gases were used for the experiment, this numerical study considers only air assumed as a perfect gas.

Numerical investigations of the single-expansion-ramp nozzle, the scramjet nozzle, and other nozzles similar to these types have been reported in the litterature [4-7]. Three-dimensional flowfields for the single-expansion-ramp nozzle have been computed for a pressure ratio NPR=10 [4]. Laminar results agreed very well with the experimental data. The simulation includes the exhaust plume which is surrounded by shear layers between the exhaust flow and the external quiescent air. For this class of mixing, in which one of the coflowing streams is quiescent, the flow eventually becomes unsteady downstream because of interaction and momentum transfer. The exhaust flow induces many circulatory vortices in the adjacent quiescent surrounding, as the flow progresses downstream and gradually loses its momentum. This unsteady behavior is characterized by formation of large-scale vortex structures and dissipation. Numerically, the unsteady flow pattern of the plume region can be modelled using a time-accurate procedure, but poses a convergence problem for a time relaxation scheme to obtain steady state solutions, such as the one formulated in the PARC code. However, there is a segment of the exhaust flow upstream near the nozzle exit where the shear layer is stable for a steady state calculation. Through numerical experimentation it has been found that the length of this segment varies depending on the characteristics of the expanding flow inside the nozzle. In general, internal flow at large pressure ratios provides stable shear layers and the unsteadiness takes place at a distance far downstream. This is the case in the previous laminar computation at NPR=10. As the pressure ratio is reduced, the free shear layer becomes unsteady earlier at a very short distance from the nozzle exit. The reason for this pressure ratio dependency is that the flow at large pressure ratios is expanded to a higher Mach number and therefore greater momentum, as compared to the flow at smaller pressure ratios. Consequently, the exhaust flow at high Mach number can penetrate farther into the quiescent surrounding before becoming unsteady. The

present study of the single-expansion-ramp nozzle, as a continuation of the previous work, examines the flowfield at a lower pressure ratio of NPR=4. The results presented here are for turbulent flow. This is one of the differences from the previous work where laminar flows were simulated without convergence difficulty. At the present pressure ratio, steady state laminar solution could not be obtained and may not even exist. Further study is required to resolve the issue. Convergence for turbulent flow, however, was obtained but required an extensive amount of computational effort. The present steady state solution indicates a flowfield which contains a three-dimensional internal shock wave on the nozzle walls and a helical streamwise vortex in the exhaust flow, in addition to other similar flow structures observed for laminar results at NPR=10 in the previous investigation.

This paper also presents the results obtained from a three-dimensional computation of a scramjet nozzle. The configuration is similar to that of the single-expansion-ramp nozzle. The difference is in the spanwise geometrical variation that leads to several viscous regions to be resolved. The flow characteristics exhibit very strong expansions in both streamwise and spanwise directions. Because of grid limitation, the exhaust plume behind the body is not modelled in this case. This assumes that the external exhaust flow has a negligible upstream influence at very high Mach numbers. A free shear layer occurs between two supersonic streams and is more stable than the ones encountered in the previous case, even though the relative velocity between the two streams is large. Another physical feature is the vortical flow over the edge of the external expansion surface. This vortex system resembles the structure observed in the flowfield over swept wings, in which the shear layer along the leading edge curls up to form a streamwise vortex. Results are presented for laminar flow, although turbulent solutions can also be obtained. Results calculated in both laminar and turbulent regimes for a two-dimensional test case have indicated no noticeable differences between the two regimes. The apparent stability of the overall scramjet flowfield leads to a minimal computational effort required for convergence.

In order to obtain accurate numerical solutions, a very large number of grid points is needed to resolve all the high gradient regions appearing in the domain. However, grid clustering in such regions is still a difficult problem, except in the case when the location of the sharp gradient regions is known in advance. Effectively resolving the free shear layer, which normally follows an irregularly curved trajectory, becomes quite complex. Although an adaptive grid can concentrate and redistribute grid points in these layers as the computation proceeds, it is not trivial in complex flows to control grid smoothness, distortion and resolution. Though success has been observed in two dimensions, three-dimensional results are still lacking. For this reason, the grid adaptation has not been implemented in the present calculations, and is a subject for future work. Free shear layers and shock waves are then not as accurately defined. Numerical error associated with the lack of resolution appears as an additional artificial diffusion which then smooths out these sharp gradient flows.

NUMERICAL METHOD

The detailed development and some of the recent work related to the PARC computer program can be found in references [1,4,8-9]. Generally, the program solves for steady state solutions of the Euler, full or thin layer Navier-Stokes equations in a generalized curvilinear coordinate system using a time marching finite-difference scheme. This numerical scheme uses standard central differences to approximate the spatial derivatives. The time linearized difference equations in a delta form are solved by the Beam-Warming ADI algorithm with diagonalization of the inviscid terms. Jameson-type artificial dissipation is added for monotonicity and stability. The resulting computational procedure then requires iteration from an initial guess for the flowfield until convergence to a steady state is obtained. Another common feature for a time-like marching technique is the use of spatially variable time steps. This is introduced to achieve faster convergence rates especially in the coarse grid areas where large time steps can be used because of a less severe restriction on stability. In the present calculations, the thin layer Navier-Stokes equations are employed. The thin layer assumption is applied since the flow is in the high Reynolds number range, in which the contribution from the streamwise diffusion terms becomes negligible. In addition, due to computer resource limitations, the grid in the the flow direction cannot adequately resolve the viscous phenomena. The neglect of these diffusion terms then produces considerable decrease in computation time, especially in three dimensions.

In the turbulent calculation, a modified Baldwin-Lomax model is employed for eddy viscosity. A modification to the original model is made to permit multiple Prandtl mixing lengths for the outer wake region, based on the vorticity distribution along individual curvilinear coordinates. This consideration for multiple length scales is particularly important when using algebraic models for flows in the presence of both wall boundary layers and free shear layers, as is the case in this study. In the modified model, each grid line is segmented at the location where the vorticity is minimum. The mixing length is then assumed to be uniform along that segment, and is determined by some ratio of the total velocity and vorticity, see ref. [1]. The wake value of turbulent viscosity is applied throughout the flowfield domain including free shear layers and the outer parts of wall boundary layers without further modification. Numerical work on this modified version, however, has not been documented extensively. The pressure distribution presented here in the region of the shock wave and boundary layer interaction shows an improved prediction of the location and strength of the shock wave as compared to laminar results. Experimental data for the free shear layer in the present investigation are not available for comparison.

For boundary conditions, all are explicitly formulated in an iterative manner. At the inflow or outflow boundaries, the conditions can be either specified or extrapolated according to the local characteristic directions. This kind of boundary treatment works effectively when all characteristics have the same direction, i.e., when boundary points are either all subsonic or supersonic and contain no reversed flow. Difficulty in convergence arises when mixed types of characteristics occur. Extrapolation at every point for boundaries having different characteristics appears to be a more stable treatment, but does not honor the characteristic

direction. However, this numerical treatment of extrapolation is implemented here at the outflow boundary. On the nozzle surfaces, no-slip and adiabatic conditions are imposed. In the farfield, the variables are fixed for the external supersonic stream, provided that the boundaries are positioned at a sufficiently large distance from the nozzle/exhaust flows. As for quiescent air, the farfield boundary is treated initially as an inflow boundary because of entrainment into the shear layer, and is then fixed in the later stage of iteration. This dual treatment of the quiescent boundary is considered as a means of relaxation for convergence and can be repeated when necessary. At the entrance of the single-expansion-ramp nozzle, only stagnation pressure and temperature are specified since the flow is subsonic. Other unknowns are computed as inflow conditions using isentropic relations and characteristic variables mentioned above. On the other hand, at the entrance of the scramjet nozzle a uniform profile is assumed, neglecting the incoming boundary layer effects. The variables at this boundary are fixed during the computation process, since the flow is supersonic. For normalization, stagnation quantities at the nozzle entrance are taken as the reference. The nozzle throat height and the speed of sound are the reference length and velocity, respectively. The Reynolds number is computed based on these parameters. For laminar flow, molecular viscosity is obtained from the Sutherland law. The laminar and turbulent Prandtl numbers are assumed to be equal to 0.72 and 0.9 respectively.

GEOMETRY AND GRID

The geometry of the single-expansion-ramp nozzle is illustrated in fig. (1) obtained directly from ref. [2]. In this study, the streamwise, vertical and spanwise directions are labeled as x, y and z respectively. The dimensions shown are in centimeters. The figure depicts the x-y or side view which lies along the streamise direction, showing a converging/diverging nozzle. In addition, there is an extra external section of the upper surface extending from the end of the lower surface. The resulting external expansion provides asymmetric exhaust flowfields and thrust deflections. The upper and lower nozzle walls are flat surfaces having no variation in the spanwise direction that is perpendicular to the x-y plane. Consequently, there is a symmetry plane in this spanwise direction and only half of the nozzle thus needs to be computed. The nozzle width-to-throat ratio is equal to 4, where the throat height is 2.54 cm. The sidewall is also indicated in the figure and is assumed to have a uniform and very small thickness of 0.007 cm. The nozzle exit along the edge of the sidewall is highly skewed as shown. The intersections of the side plate with the nozzle walls occur slightly ahead of the ends of the surfaces. The configuration computed here was labeled as case OT5 in the experiment. For this configuration, one of the intersections is found at the same location as that of the end of the lower surface. The other intersection is measured at 1.708 cm upstream of the end of the upper surface. This detail complicates the simulation only to a small degree.

The overall geometry of the scramjet nozzle is illustrated in fig. (2a). Another view with dimensions is presented in fig. (2b) for the x-y plane. Similar to the single-expansion-ramp

nozzle, the model includes a short cowl and a long ramp as the upper and lower surfaces shown in the figure, respectively. In the present computation, the ramp angle is 20 degrees. The interior side of the cowl also has a minor expansion ramp, see fig. (2b), with an angle equal to 12 degrees. In the spanwise direction, the nozzle geometry consists of a reflection plate on one side of the flowfield, and a short sidewall to contain the internal flow before exiting to expand. The short sidewall has a flat surface facing the internal flow. The sidewall external surface facing the free stream flow is tapered. The sidewall and the cowl therefore both have finite thicknesses with sharp trailing edges. The flow fence connected to the short sidewall, as indicated in the figure, is not simulated in this study. The nozzle width-to-throat ratio is equal to 5, with the throat height of 0.6 inch at the combustor exit. The long ramp surface can be divided into two regions with nearly equal lengths in the spanwise direction. The interior region next to the reflection plate includes the flow between the reflection plate and a streamwise x-y surface containing the sidewall. The exterior region includes the flow between this surface and the freestream. The flow in the exterior region appears to have a simple flow pattern due to just an expansion over a 20-degree ramp. However, because of spanwise expansion outward from the interior side as well as inward from the freestream side, the flow in the exterior region of the ramp surface is a rather complex system characterized by developing streamwise spiral vortices. The computational domain simulated here begins at the combustor exit. The flow effects prior to this location, such as from the action of boundary layers or embedded waves, are ignored for simplicity. This aspect of the boundary effects on the accuracy of the solution will be discussed further in the following section on the numerical results.

The corresponding three-dimensional grid distributions are illustrated in figs. (3a) and (4a) for the single-expansion-ramp and scramjet nozzles respectively. Two-dimensional close-up views on x-y planes are shown in figs. (3b) and (4b). In the figures, some of the grid points have been removed for clarity. These grids were generated by a simple algebraic technique using a hyperbolic tangent for grid clustering in the region near walls. In the spanwise direction, the x-y grids are stacked without variation, i.e., in that the cartesian coordinates, x and y, are not functions of the spanwise transformed curvilinear coordinate. Concentrations in this direction are applied at the sidewalls, as in the middle of the single-expansion-ramp nozzle or along the reflection plate, the short sidewall, and the model edge of the scramjet nozzle. It can be observed that the clustering in the viscous regions near the nozzle walls are extended farther downstream into the wakes behind these surfaces. The clustered regions in the wake become unnecessary since the paths of the shear layer normally do not follow the clustering. This is a typical behavior of structured H-grid distributions, in that the interior grid distribution is affected by the surface grid refinement. However, there are several alternative methods, e.g., simple averaging, which can be employed in the wakes to alter the distribution, but are not pursued in this study. For surface grid coordinates, a cubic spline procedure is used to interpolate between the tabulated data describing the nozzle contours. This interpolation to position grid points is applied for the internal contours of the single-expansion-ramp nozzle. Other surface contours are straight lines which can be easily implemented. Another remark is that the vertical grid lines in the middle section

are highly nonorthogonal to the horizontal coordinate, see fig. (3b), but are made to align with the edge of the sidewall in order to simplify the boundary condition application. The grid dimension for the single-expansion-ramp nozzle is 95x90x50, whereas for the scramjet nozzle, the grid has a dimension of 90x90x95. The additional grid used in the scramjet nozzle calculation is needed to resolve four viscous boundary layers in the spanwise direction. In the figures discussed below, the i, j, and k notations denote the grid indices corresponding to the x, y and z directions, respectively.

RESULTS

Single-Expansion-Ramp Nozzle

Numerical results are presented for a turbulent, thin layer Navier-Stokes calculation. Flow through the domain is initiated by a pressure difference between the nozzle entrance, at a total pressure of 405.2 kPa and a total temperature of 300 K, and the quiescent ambient, at a pressure of 101.3 kPa and the same total temperature of 300 K. The stagnation-to-static nozzle pressure ratio, NPR, is therefore equal to 4, and the corresponding Reynolds number obtained for these conditions is 2,251,500.

Starting from a near zero velocity at the entrance, the generated flow becomes sonic at the throat, expands supersonically along the diverging section with the existence of a shock wave, and exhausts supersonically into stationary air. Figures (5a-7c) describe this overall flowfield in terms of Mach number contours, indicating some of the important physical features. The contours cover the entire range of the Mach numbers with an equal increment. Depicted in these figures are the side, top and rear views at various spatial locations. Flow expansion along the streamwise diverging/ converging sections is shown in figs. (5a-c) at three different spanwise locations, moving from the center plane to the sidewall. The pattern consists of a rapid expansion at the throat, and an oblique shock wave with its reflection below the boundary layer on the external section of the upper surface. The lower shear layer acts as a fictitious nozzle wall to complete the diverging section. The shock wave is a result of coalescence of the compression waves formed by the curvature of the lower shear layer. The thickening of the boundary layer behind the shock can be observed. The reflected shock then interacts with the lower shear layer, creating a reflection of expansion waves at the other side of the corner. This lower shear layer gradually diminishes toward the sidewall, resulting from the inward deflection of the vertical shear layer. The maximum Mach number is 1.935 and located in front of the shock near the symmetry plane. The flow behind the shock is nearly sonic, except for a thick subsonic region adjacent to the wall where the shock becomes normal.

Streamwise variations of Mach number can also be seen from the top views in figs. (6a-b). The top boundary is the center line, and the sidewall is in the middle of these figures. The corresponding mixing layers emanate from the sidewall trailing edges. The view in

fig. (6a) is at a vertical location near the nozzle center, also showing a rapid expansion at the throat, and compression waves near the sidewall edge. The other view in fig. (6b) is at a vertical location near the upper surface, having a similar pattern except that the compression waves now coalesce into a shock wave which can be seen clearly. This shock wave also interacts with the boundary layer along the sidewall. Another feature present in these figures is the deflection angle of the shear layer from the sidewall. The shear layer in fig. (6a) is deflected toward the internal nozzle region, due to a low pressure from the inside. On the other hand, the shear layer in fig. (6b) is deflected toward the external nozzle region, due to higher pressure behind the shock wave. Therefore, the exhaust flow along the sidewall is both underexpanded and overexpanded in the regions near the lower and upper surfaces, respectively.

Another two-dimensional view of the three-dimensional shock surface can be seen from the rear in figs. (7a-c). These figures illustrate the cross sections at different streamwise locations. It should be noted that the top views, figs. (6a-b), and the rear views, figs. (7a-c), are projections of the curvilinear coordinate planes onto x-z and y-z cartesian planes, see the grid distributions in figs. (3a-b). The symmetry plane is the right boundary in figs.(7a-c). Fig. (7a) is at a streamwise location near the edge of the sidewall, where both nozzle walls are shown. Shock wave and boundary layer interaction can again be seen near the upper surface by the apparent thickening of the viscous regions along the sidewall and the upper surface. Fig. (7b) is located at the external section, showing the initial regions of the vertical and lower shear layers. The reflected shock has moved downward to the middle and becomes diffused. An example of the Mach number contours in the exhaust plume behind the nozzle is depicted in fig. (7c), where only free shear layers are present. The vertical shear layer indicates an irregularly curved sheet of high velocity gradient, as compared to the relatively well-defined upper and lower layers. The lower left-hand intersection of the shear layers is the center area of a helical streamwise vortex.

Typical variations of pressure, density and temperature are presented in figs. (8-11) for the side and top views. Figs. (8-9) show the pressure and density contours near the symmetry plane. There is no variation in pressure and a small gradient in density across the shear layer. These figures indicate a regular pattern of multiple shock cells usually observed in the exhaust flow. In addition to a region of concentrated vorticity, the shear layer in compressible flows also manifests itself through a steep variation of temperature. This associated thermal layer can be seen in the temperature contours in figs. (10a-b) plotted for two vertical locations near the nozzle middle and the upper surface. Similar contour patterns show shock wave, large temperature gradient and deflection of the thermal shear layer. Figs. (11a-b) illustrate the pressure contours for the same view and the same vertical locations as for temperature above. These figures detail the repeated cycles of a shock/compression and expansion wave reflection.

The vortical systems of the exhaust flowfield are demonstrated in the next three figures. The velocity vectors are plotted in fig. (12) for a spanwise cross section located a few stations downstream of the nozzle body. The symmetry plane is now the left boundary, and the dense regions of closely packed vectors arise because of grid clustering along the upper,

lower and sidewall surfaces. The pronounced structure clearly identified is the counter-clockwise vortex, centered near and inside of the nozzle upper right-hand corner in the figure. The vortex system rotates at higher angular velocities in the sidewall vicinity than in other regions, as suggested by the lengths of the velocity vector. The vortex occupies a large spanwise area of the plume flowfield, and the entire expanding fluid medium exiting from the nozzle, consequently, undergos a streamwise vortical motion. Another smaller vortex having the same sense of rotation also exists, with its center near the lower right-hand corner of the nozzle. The longitudinal view of this streamwise vortex is shown in fig. (13) in three dimensions, illustrating the trajectories of the particles released at the nozzle entrance along the lower, sidewall and upper internal surfaces. The vortex system is represented by the clustered spiral paths of the fluid particles originating behind the nozzle lower corner. Trajectories at the upper corner are deflected downward by the presence of a very small separated bubble. Other trajectories away from the sidewall remain in the regions of shear layers. Another view of the small streamwise vortex with the apex at the nozzle lower corner is illustrated in fig. (14). This is a view looking upstream along the axis of the vortex. Spiraling motion of the fluid particles along the vortex is evident.

Figures (15a-b) compare the computed and measured pressure distributions for the upper and lower surfaces at the symmetry plane. The agreement is very good. The strength and location of the shock wave appearing in the external section of the upper surface are well predicted. The computed discharge coefficient of 0.989 also agrees reasonably with the experimental value of 0.974. In this calculation, the smallest grid size is employed at the walls and is of the order of 0.001. This gives values of y^+ and z^+ in the range of 10 at the first grid point from the wall, and typically 4 subsonic points in the viscous layers.

Convergence is rather difficult to achieve and very sensitive to the time step. The use of a different time step for the energy equation and an underrelaxation for the eddy viscosity somewhat reduces the fluctuating behavior of the residuals. The solution presented here for the single-expansion-ramp nozzle was obtained after a residual reduction of three orders of magnitude in approximately 10,000 iterations. A large number of these iterations was used for the reduction of the last order of magnitude. Further reduction of the residual beyond this level is still possible but becomes prohibitively slow. Each iteration took 16 seconds, and the total computation time required 45 hours on a Cray-2.

Scramjet Nozzle

The solution computed for the scramjet nozzle is obtained from the laminar, thin layer Navier-Stokes equations. The inflow boundary condition at the nozzle entrance is assumed to be a uniform profile at a Mach number of 1.62, a pressure of 3.408 psi and a total temperature of 150 F. The freestream is also assumed fixed and uniform at a Mach number of 6, a pressure of 0.226 psi and a total temperature of 400 F. The static pressure ratio is then equal to 15.09, and the Reynolds number based on this condition is 293,300.

Variations of Mach number of the scramjet nozzle are illustrated in figs. (16a-c) for side views at three spanwise locations. Fig. (16a) shows the contours at a location between the

reflection plate and the short sidewall, where the flow is nearly two-dimensional. The internal flowfield is characterized by a strong expansion beginning with two opposite expansion fans emanating at the entrance lower corner and from the upper corner under the cowl surface. The expansion then continues behind the fans over the long ramp, and accelerates the flow to a Mach number of about 5.6 in the ramp rear-end vicinity, a value close to the freestream Mach number. Above the internal expanded flow is a mixing layer emerging from the cowl lip. Even with a large pressure drop behind the expansion fans, the exhaust flow still remains underexpanded. The shear layer consequently turns upward to the external side at the lip, and remains almost horizontal downstream. However, the angle of deflection is small, and the resulting shock wave as well as expansion fan on opposite sides of the shear layer are relatively weak. This shock wave which originates from the cowl lip can be seen clearly in the external flow, but the expansion fan below the shear layer cannot be discerned from other flow features. Along the free shear layer several other waves are also emitted into the external stream, as a result of pressure adjustment to the freestream usually exhibited in supersonic mixing layers. Additionally, an oblique shock wave exists at the cowl leading edge of the upper surface, occurring here solely because of the boundary layer. Fig. (16b) presents the Mach number contours at a spanwise location very close to the short sidewall, depicting a similar structure of the flowfield. The vertical concentration of contours at the cowl lip is an indication of the mixing layer behind the trailing edge of the short sidewall. The internal flow between the entrance and this trailing edge lies within the subsonic region of the sidewall boundary layer, showing an irregular pattern of Mach number contours without the expansion fans observed before. The external region of the ramp surface, fig. (16c), shows simple flow turning over a 20 degree corner with expansion waves at the leading edge. Next to the wall, the flowfield is more complex containing a thick viscous region with embedded streamwise vortices formed by the interaction of internal and external streams. Fig. (17) represents a typical variation of the density contours for a side view located between the reflection plate and the short sidewall. The wave system exhibited here is more discernible than it is illustrated by the Mach number contours. The pressure and temperature contours contain no other significant physics, but have similar patterns as density and Mach number contours, respectively. They are not included here due to space limitation.

Top views for Mach number contours are illustrated in figs. (18a-c) at various vertical locations with the flow from left to right. The sidewall is shown as a thin splitter plate in figs. (18a-b). The flow pattern in fig. (18a) lies within the boundary layer along the ramp surface, illustrating some of the spanwise expansion of the internal flow. It has been found from the solution that the fluid layer nearest to the wall experiences the largest spanwise expansion. The clustering of the contours at the top of the figure is an indication of the viscous effect of the boundary layer along the edge of the model. This effect diminishes when the vertical position is at a higher level as shown in fig. (18b) located near the cowl internal surface. The shear layer emerging behind the sidewall edge is indicated as the horizontal clustering, depicting a small spanwise expansion at this particular vertical location. Another clustering at the bottom of the figure is the boundary layer along the reflection plate. The vertical contour concentration represents the expansion fan due to the deflection of the shear

layer originated along the cowl lip. At a higher vertical location far above the cowl, the flow structure becomes very simple as a supersonic flow over a reflection flat plate, and this is illustrated in fig. (18c).

A typical density distribution is presented in fig. (19) for a top view a few stations below the internal cowl surface. The expansion fan centered at the leading edge of the ramp surface is indicated. The solution shows a gradual smearing consisting of several separate contours in front of and behind the fan. It is noted that the top views, figs. (18a-19), are the projections onto an x-z cartesian plan. The rear views are presented in figs. (20a-c) for Mach number contours at different streamwise locations, and in fig. (21) for density distribution located at the middle of the ramp. Fig. (20a) is plotted for a station just behind the trailing edges of the cowl and the short sidewall. This figure shows a thickening region above the viscous layer on the external ramp surface, and the interaction of the vertical shear layer with this region. The interaction continues and enlarges downstream, illustrated in figs. (20b-c), as the lower part of the vertical shear layer near the ramp surface becomes diffused, deflects to the external side, and merges with another shear layer arising from the model edge. This additional shear layer eventually rolls up from the freestream flow to form an external streamwise vortex centered at the corner of the ramp surface and the model edge. Fig. (20c) also shows a thickening region of the boundary layer in the middle of the ramp surface proceeding downstream, indicating the formation of another smaller, flat internal vortex system. The external vortex along the the model edge is illustrated in better detail in fig. (22), showing a projection of the velocity vector on a spanwise plane at the middle of the ramp. The reflection plate here is the left boundary. The main feature in this figure depicts a large vortical structure, comprised of an expansion from the internal flow, and a turning of the external flow. The vortex center at low pressure is located at the model corner, as the fluid from the vicinity is drawn toward it. The concentration of vectors occurs in regions of grid clustering along the cowl, the short sidewall and the model edge, shown near the top, left and right boundaries of the figure.

Trajectories for fluid particles located next to the ramp surface and released from the internal side are shown in three dimensions in fig. (23). The external streamwise vortex along the model edge is represented by the spiral paths of the particles which emerge immediately behind the short sidewall and then follow a very strong spanwise expansion toward the model edge corner, where the particles are deflected into a vortex motion by the high freestream pressure side of the curved shear layer. The other internal vortex forms downstream of the short sidewall near the middle of the ramp, indicated by the clustered wavy trajectories. It can be observed that, adjacent to this vortex in the ramp middle, many even smaller vortices start to develop downstream near the outflow boundary. Another apparent phenomenon present in this figure is the delay of spanwise expansion for the fluid layers near the reflection plate, where the particles follow straight trajectories and only turn inward when they are near the outflow boundary.

Comparisons of the computed and measured pressure are made in figs. (24a-b) for the streamwise ramp-surface at two spanwise stations. Fig. (24a) is at a section near the reflection plate, and demonstrates very good agreement with experimental data, showing

the variation from the nozzle entrance to the end of the ramp. A small pressure rise near the entrance is present because of the impingement of the shock wave which originates from the leading edge of the internal cowl surface. In general, the computed pressure near the reflection plate agrees very well with the measurements. It then appears that a uniform internal profile at the entrance does not significantly alter the flowfield downstream.

Computed pressure does not agree well with measurements in the external region of the ramp surface, as illustrated in fig. (24b). The distribution shows a large pressure drop behind the expansion corner at the inflow, and then remains nearly constant without recovering back to freestream pressure, in contrast to the experimental data. As mentioned before, the uniform freestream profile does not account for earlier effects of the incoming flow occuring in front of the inflow boundary. Because of these previous effects, the external Mach number can be lower than the value of 6 employed here, and consequently the pressure drop across the expansion fan then becomes smaller and probably provides a better agreement. The discrepancy observed in the pressure of the external side can, therefore, be attributed to the error inherent in the uniform profile used at the inflow.

In this scramjet computation, the smallest grid size at the walls was of the order of 0.001, giving typically 3 subsonic points in the predominantly supersonic boundary layers. The computation is very stable requiring no special numerical treatment. After an optimum time step was selected by experimentation, convergence was straightforward and fast with no difficulties encountered during the computation. The results presented were obtained after a residual reduction of five orders of magnitude in approximately 3000 iterations. Each iteration for the scramjet simulation took 22 seconds and the total amount required 18 cpu hours on a Cray-2.

CONCLUSIONS

Three-dimensional simulations have been presented for nonaxisymmetric nozzles. Solutions to the thin layer Navier-Stokes equations were obtained with the PARC code. Turbulent calculations were performed for a single-expansion-ramp nozzle with supersonic exhaust flow in a quiescent ambient. Complex interactions between shock/compression or expansion waves and the viscous free shear or boundary layers constituted the fundamental patterns of the flowfield. Another significant structure was the vortical flow associated with two principal vortices in the exhaust plume. One of the vortices was helical with an apex at the exit of the nozzle lower corner. The other larger vortex involved the entire exhaust region behind the nozzle.

Laminar calculations were performed for a scramjet nozzle with supersonic internal and external Mach numbers. The scramjet flowfield was characterized by strong streamwise and spanwise expansions along with a dominant vortical flow. The principal large vortex, formed below the shear layer, spirals along the model edge. Other smaller and flat vortices develop later downstream near the outflow boundary. Computed wall pressure distributions, in general, compare reasonably with the experimental data for both nozzle configurations.

Shock location and strength are correctly predicted for the single-expansion-ramp nozzle. Discrepancy is observed in the external side of the scramjet nozzle, where inflow effects become important such that a uniform inflow profile may not be a good approximation.

ACKNOWLEDGMENTS

This work was supported by the NASA Lewis Research Center under contracts NAS3-24105 and NAS3-25266 with Dr. Meng-Sing Liou as monitor. The author thanks the NAS System Division of NASA Ames Research Center for the Cray-2 time. Appreciation is also expressed to M. Barton, Sverdrup Technology, Inc., for reviewing with many helpful comments.

REFERENCES

1 Cooper, G. K., "The PARC code: Theory and Usage," AEDC-TR-87-24 (1987).

2 Re, R. J., and Leavitt, D. L., "Static Internal Performance of Single- Expansion-Ramp Nozzles with Various Combinations of Internal Geometric Parameters," NASA TM 86270 (1984).

3 Cubbage, J. M., and Monta, W. J., "Surface Pressure Data on a Scramjet External Nozzle Model at Mach 6 Using a Simulant Gas for the Engine Exhaust Flow," NASP CR 1058 (1989).

4 Lai, H., and Nelson, E., "Comparison of 3D Computation and Experiment for Non-Axisymmetric Nozzles," AIAA-89-0007 (1989).

5 Baysal, O., Engelund, W. C., and Tatum, K. E., "2D Navier-Stokes Calculations of Scramjet Afterbody Flowfields," NASP CR 1034 (1988).

6 Bergman, B. K., and Treiber, D. A., "The Application of Euler and Navier- Stokes Methodology to 2D and 3D Nozzle-Afterbody Flowfields," AIAA paper 88-0274 (1988).

7 Peery, K. M., "Non-Axisymmetric Nozzle/Aftbody Flow Field Analysis," AFWAL-TR-81-3406 (1981).

8 Pulliam, T. H., "Euler and Thin Layer Navier-Stokes Codes: ARC2D, ARC3D," Notes for Computational Fluid Dynamics User's Workshop, The University of Tennessee Space Institute, Tullahoma, Tn., UTSI Pub. E02-4005-023-84, pp. 15.1 -15.85 (1984).

9 Beam, R. M., and Warming, R. F., "An Implicit Factored Scheme for the Compressible Navier-Stokes Equations," AIAA Journal, Vol. 16, pp. 393-402 (1978).

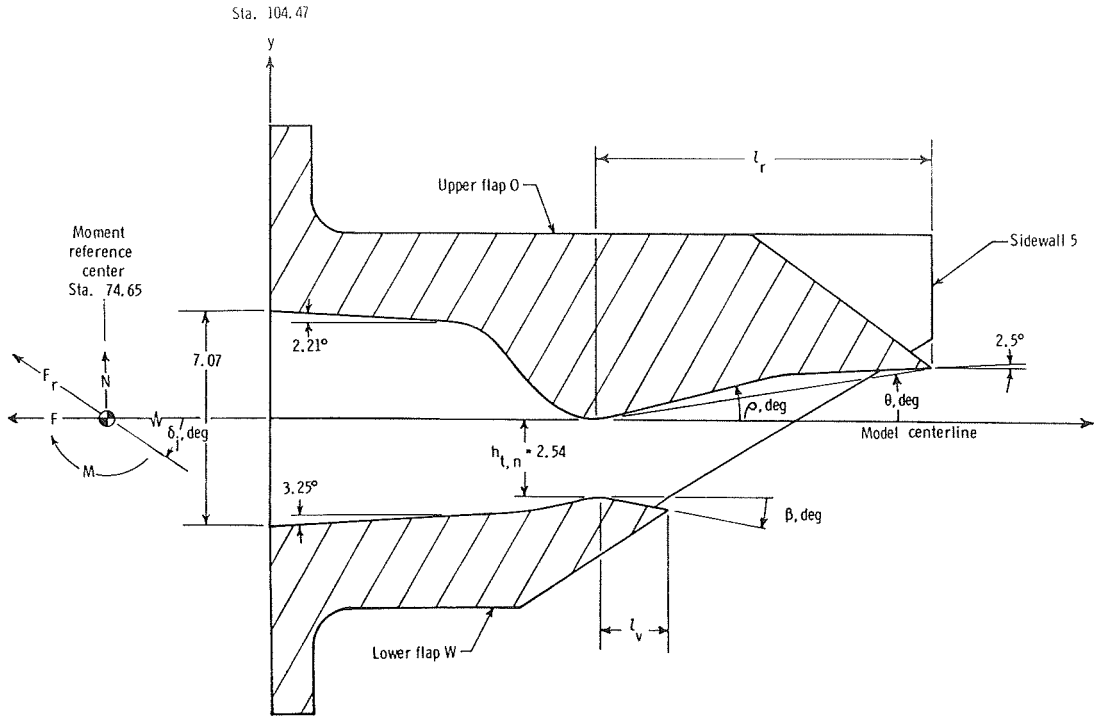

Fig. 1 Geometry of the Single-Expansion-Ramp Nozzle

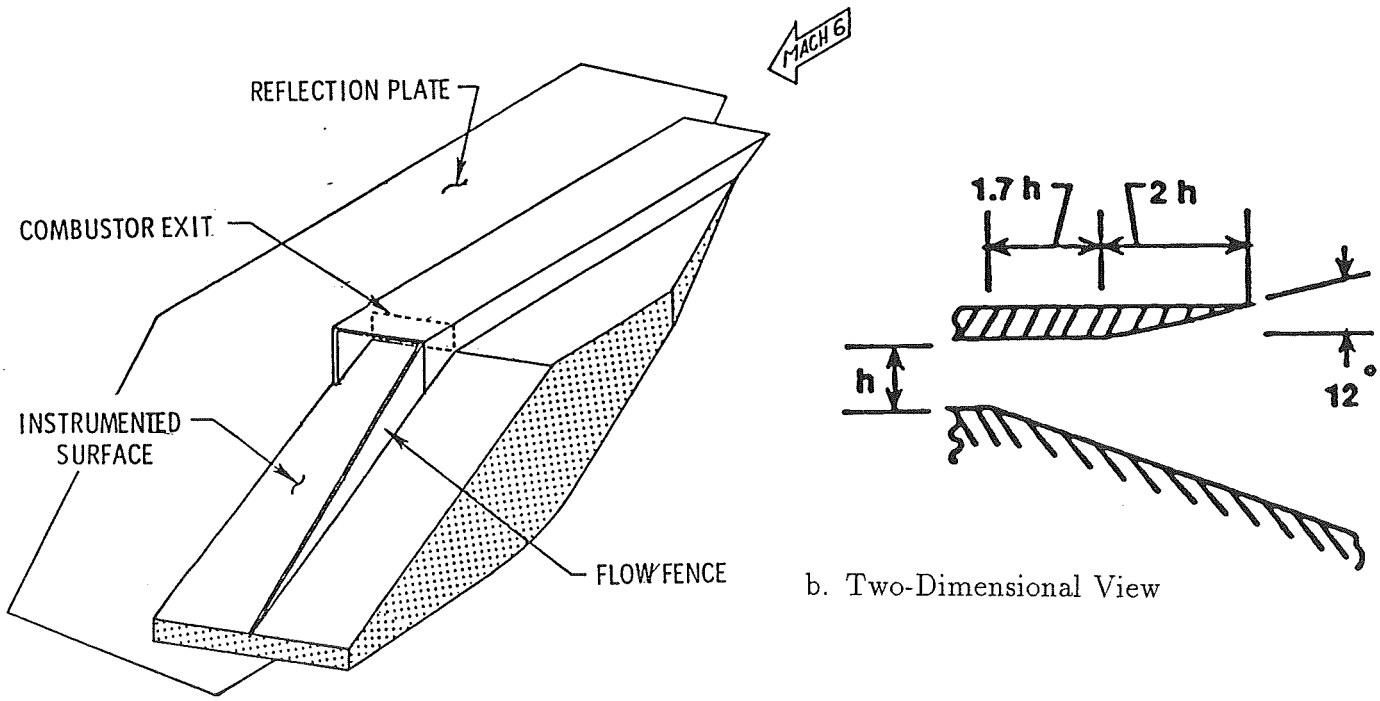

a. Three-Dimensional View

b. Two-Dimensional View

Fig. 2 Geometry of the Scramjet Nozzle

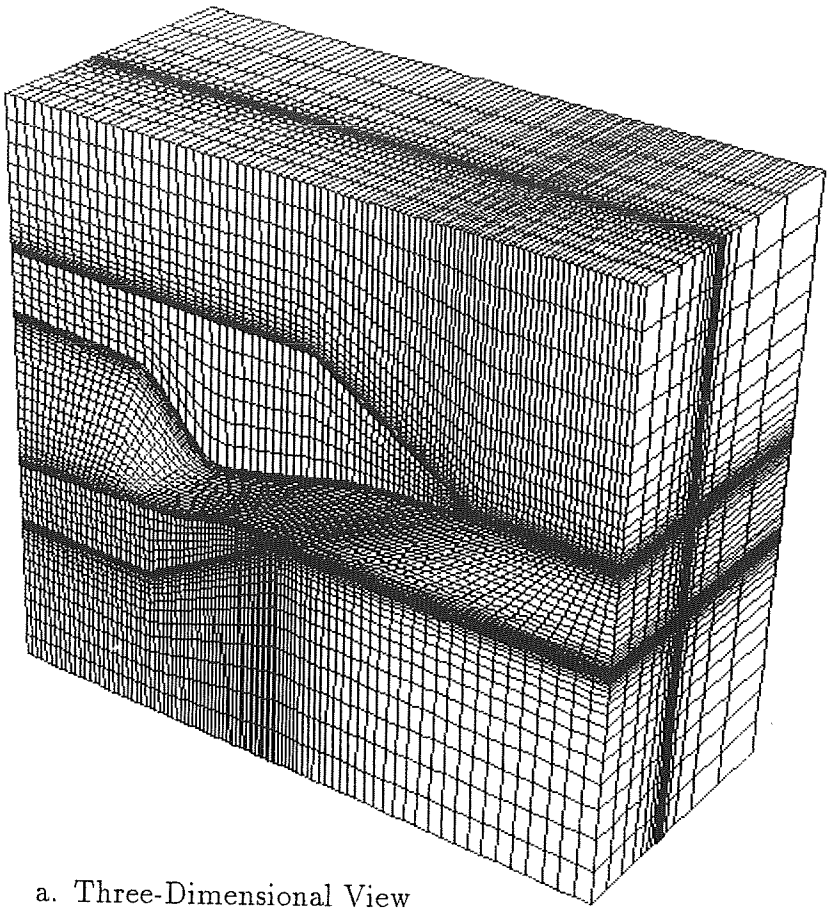

a. Three-Dimensional View

Fig. 3 Grid Distribution

Single-Expansion-Ramp Nozzle

b. Two-Dimensional View

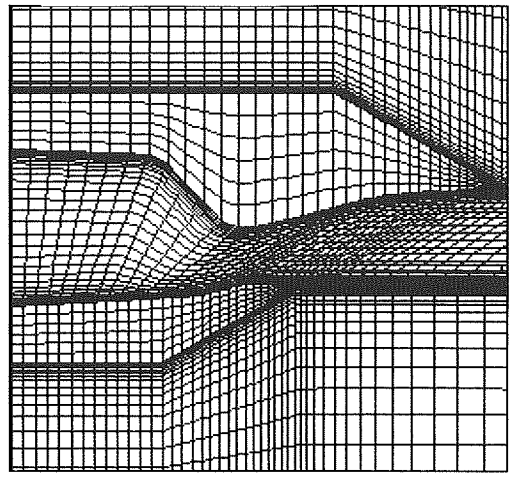

Fig. 4 Grid Distribution

Scramjet Nozzle

a. Surface and Boundary Grid

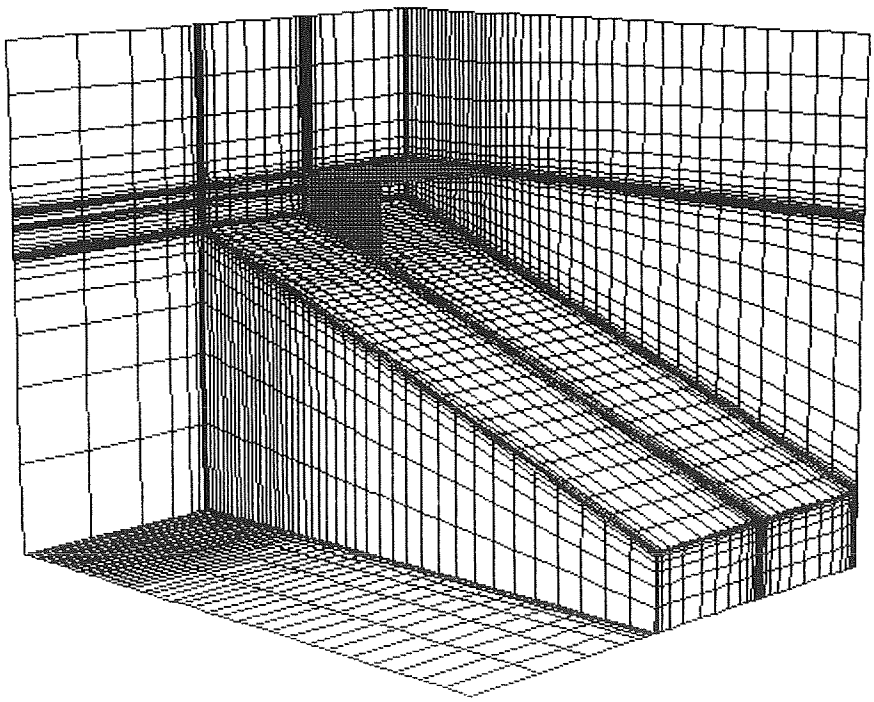

b. Two-Dimensional View

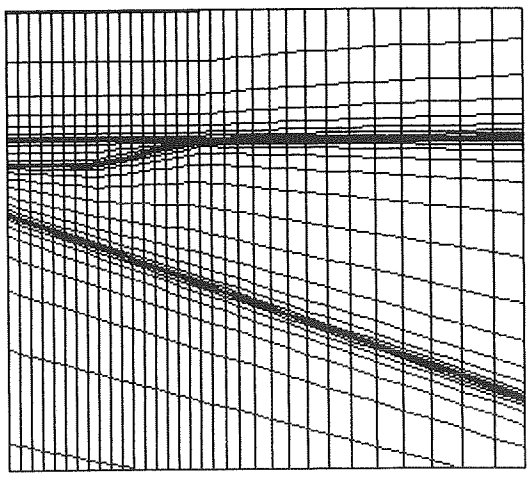

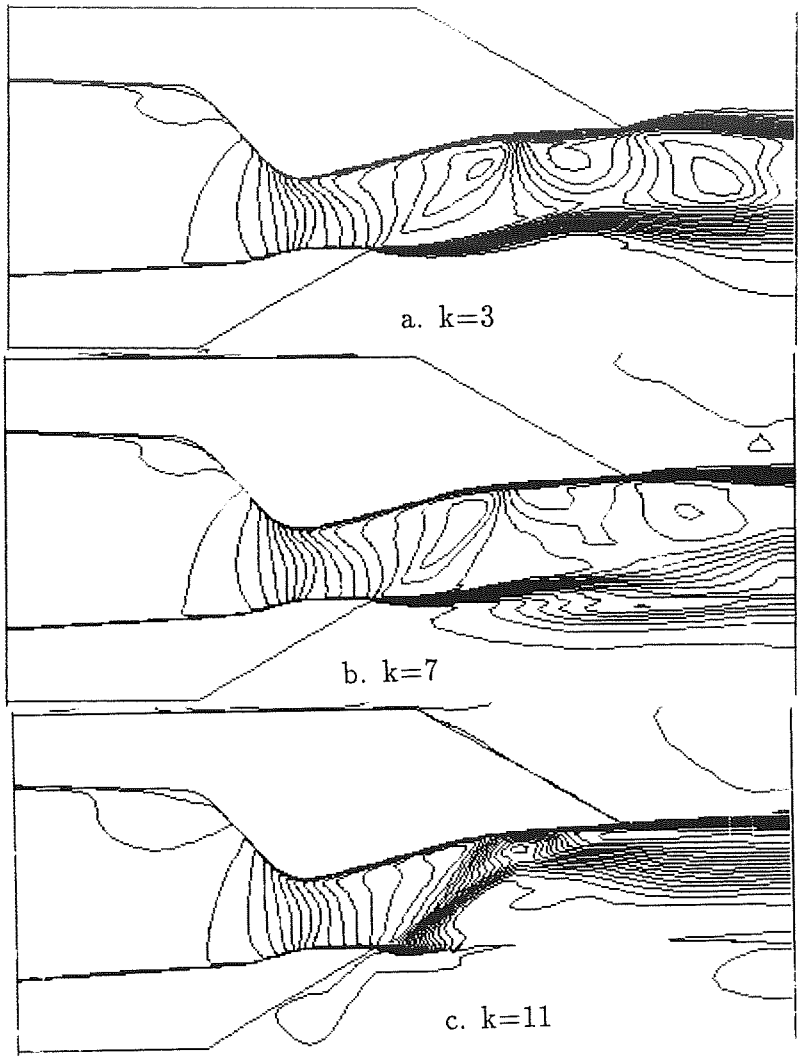

Fig. 5 Mach Number Contours, Side Views

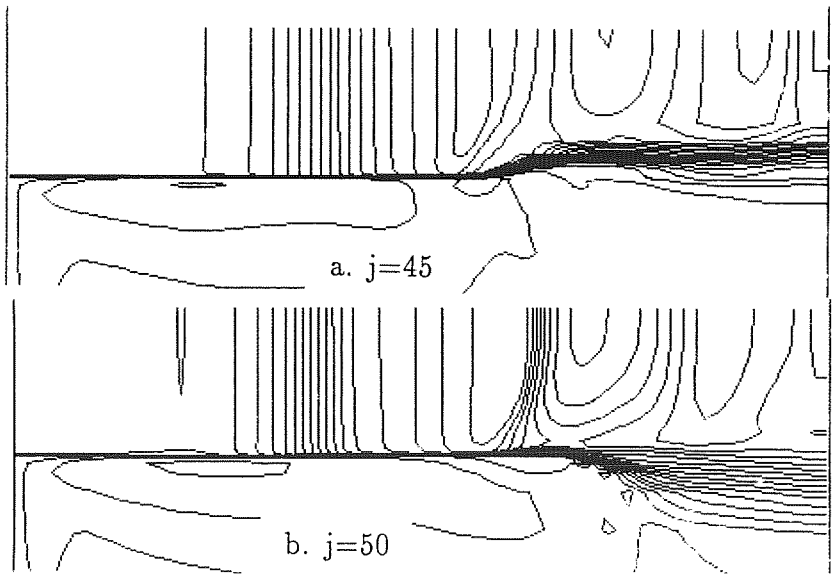

Fig. 6 Mach Number Contours, Top Views

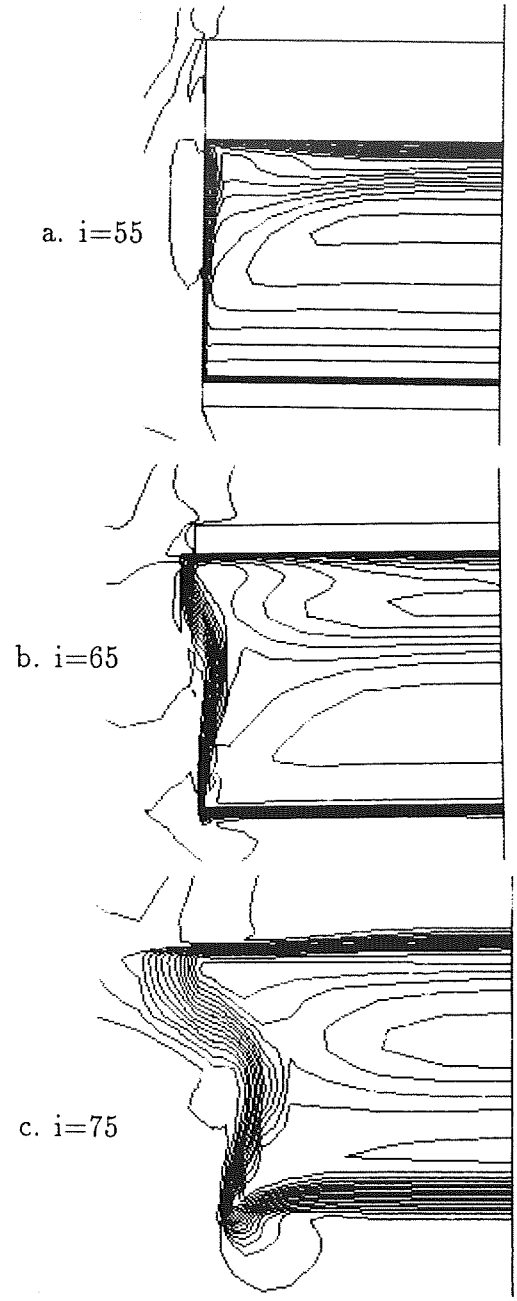

Fig. 7 Mach Number Contours, Rear Views

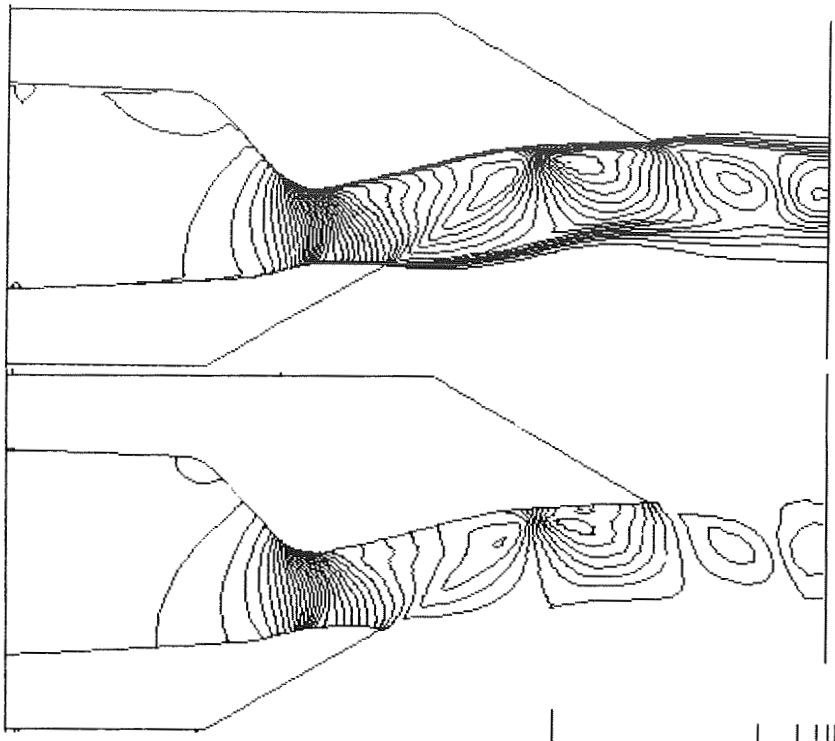

Fig. 8 Density Contours, Side View
k=3

Fig. 9 Pressure Contours, Side View
k=3

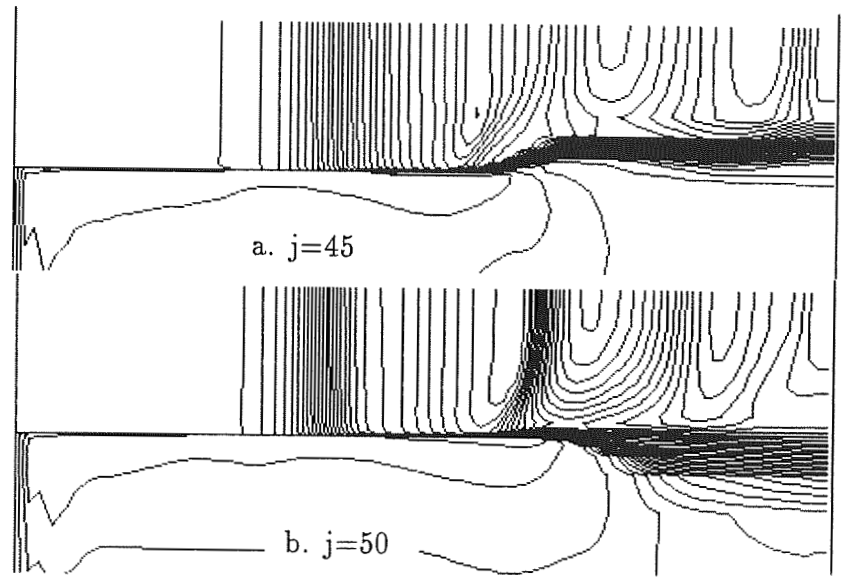

Fig. 10 Temperature Contours,
Top Views

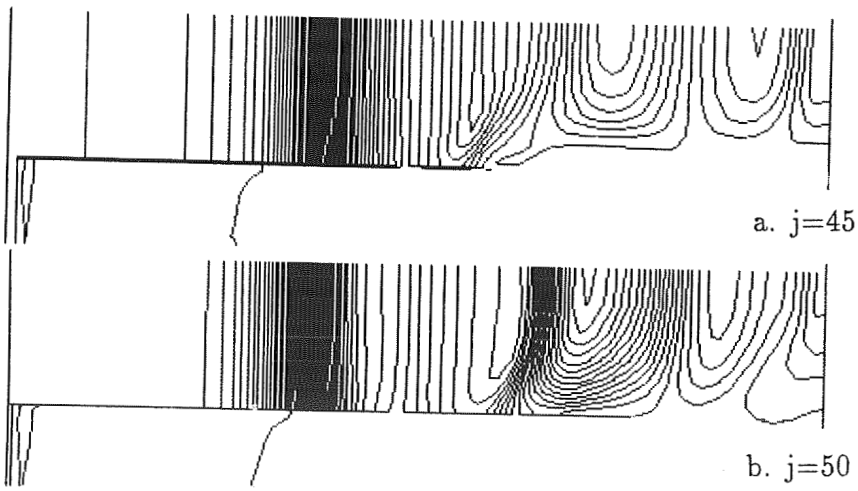

Fig. 11 Pressure Contours,
Top Views

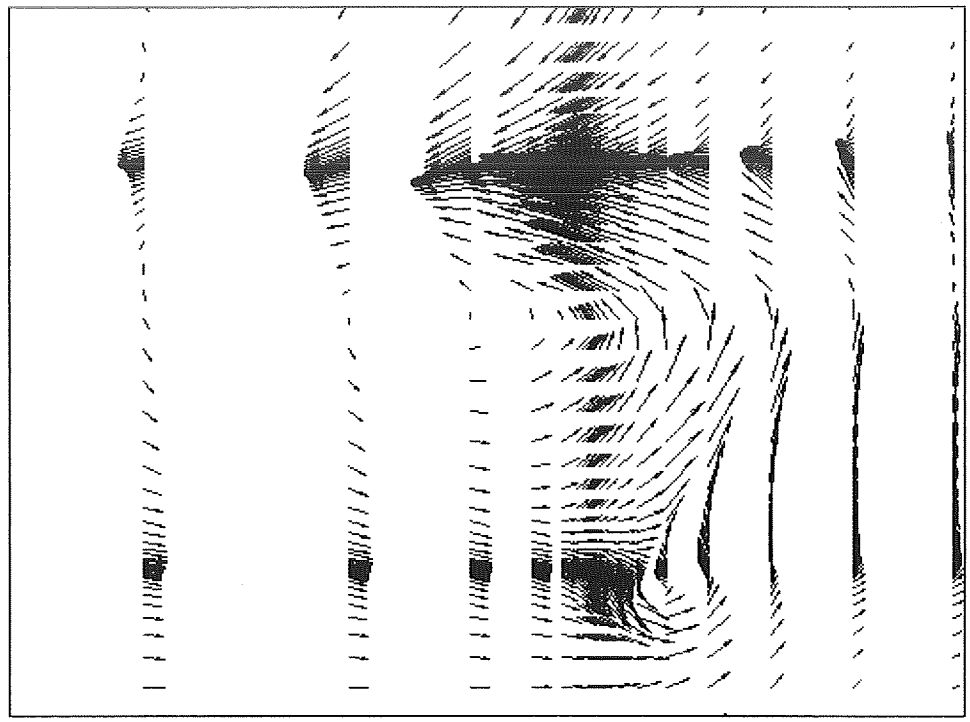

Fig. 12 Spanwise Total Velocities, i=75

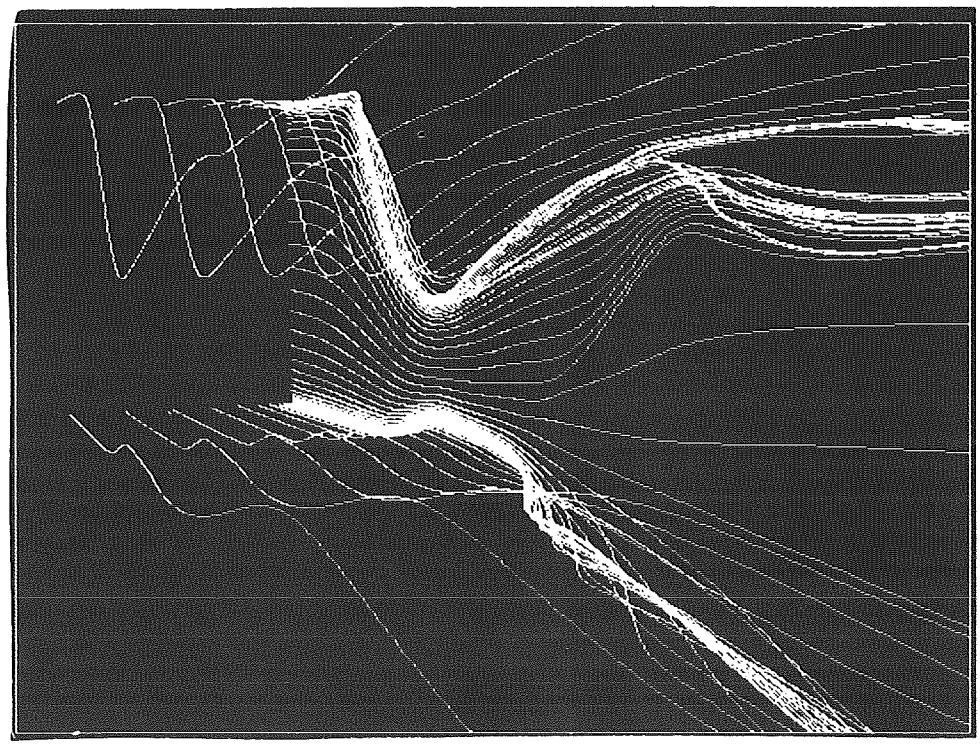

Fig. 13 Particle Trajectories, Side View

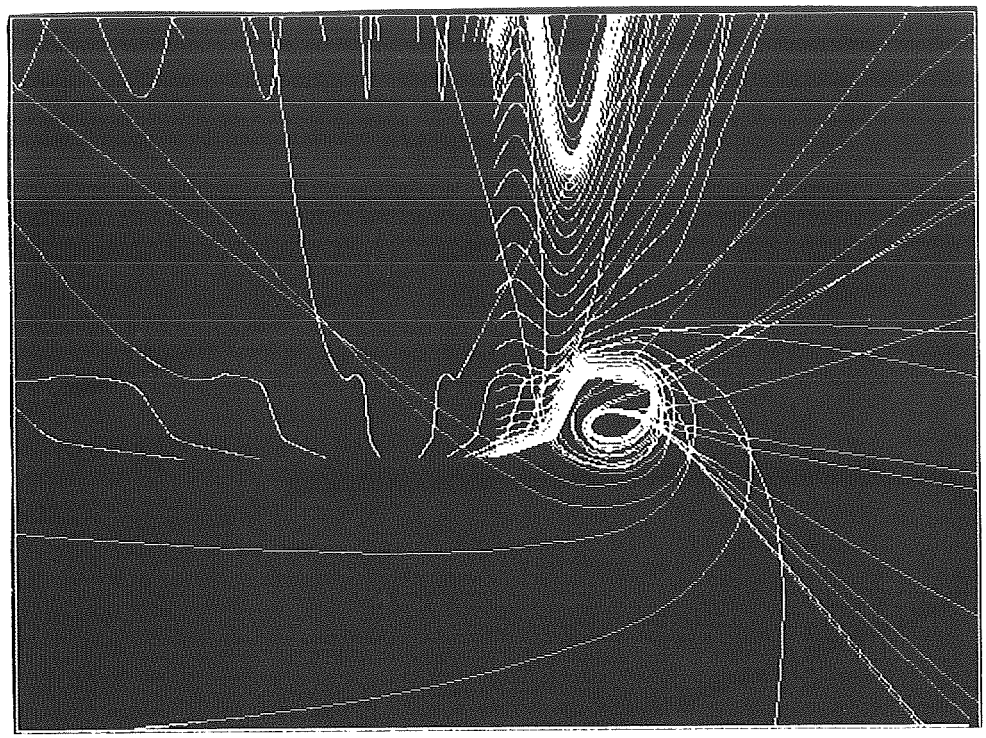

Fig. 14 Particle Trajectories, Rear View

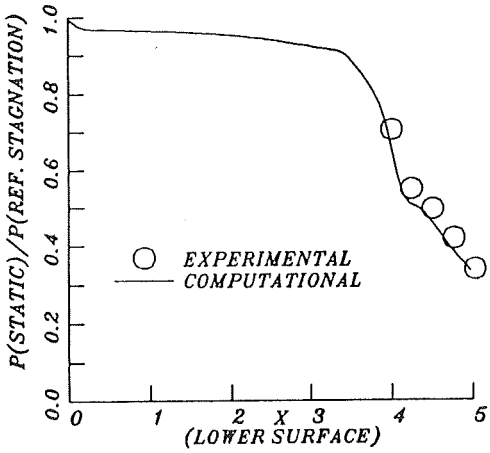

Fig. 15 Wall Pressure Distributions

a. Lower Wall

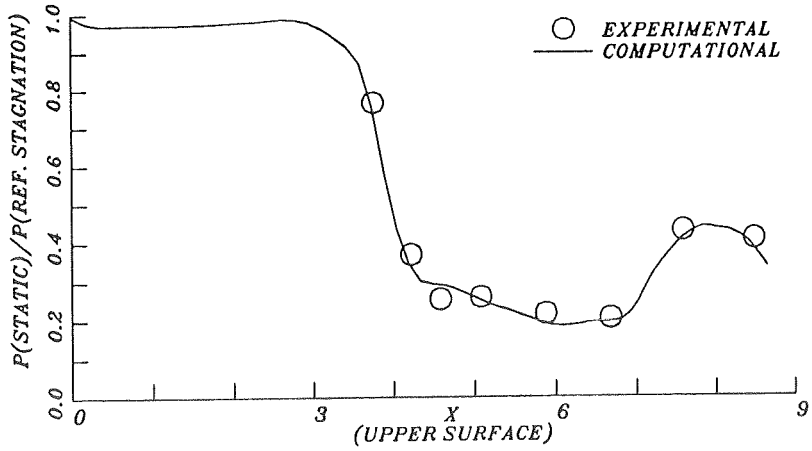

b. Upper Wall

Fig. 16 Mach Contours, Side Views

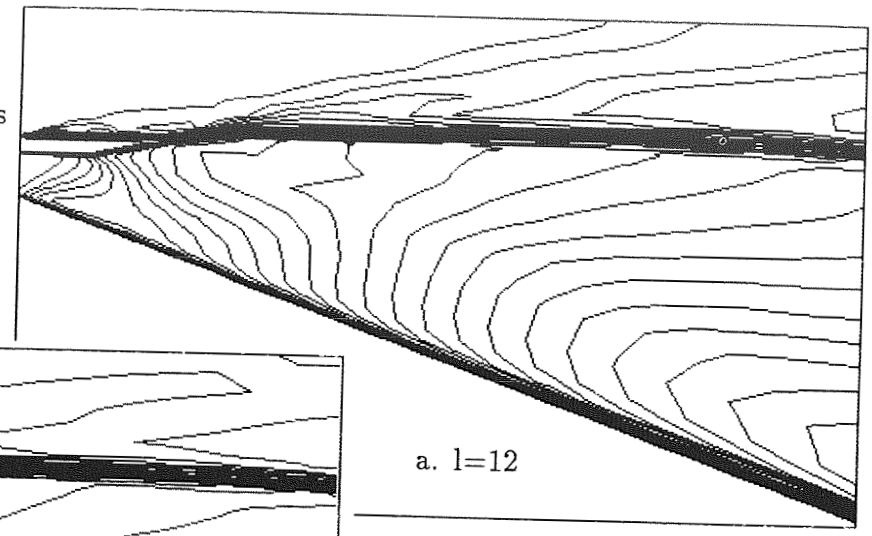

a. l=12

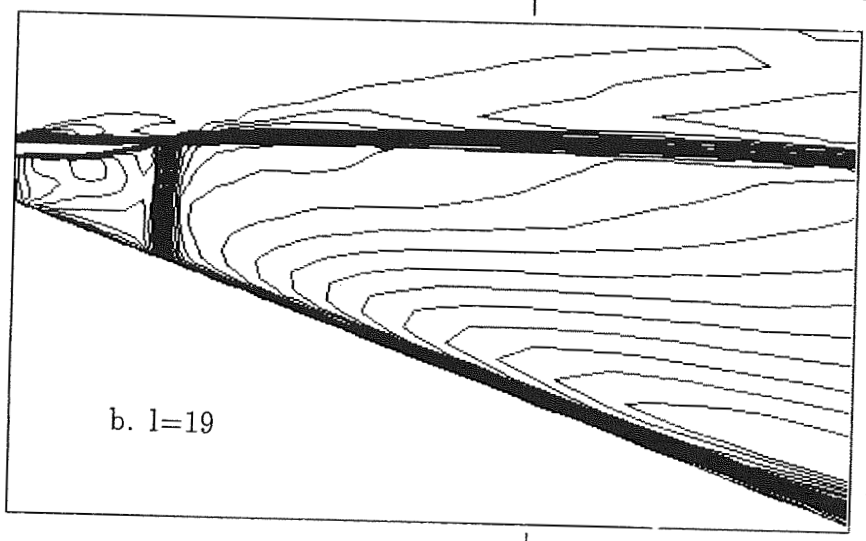

b. l=19

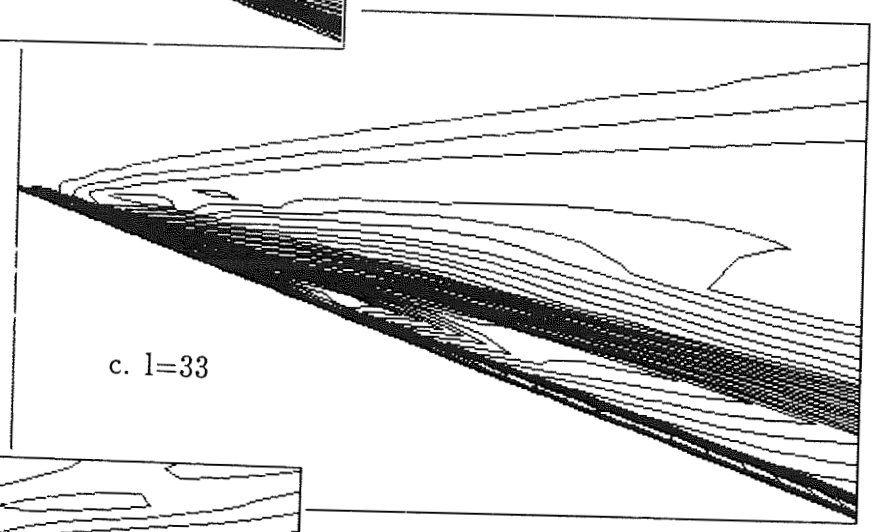

c. l=33

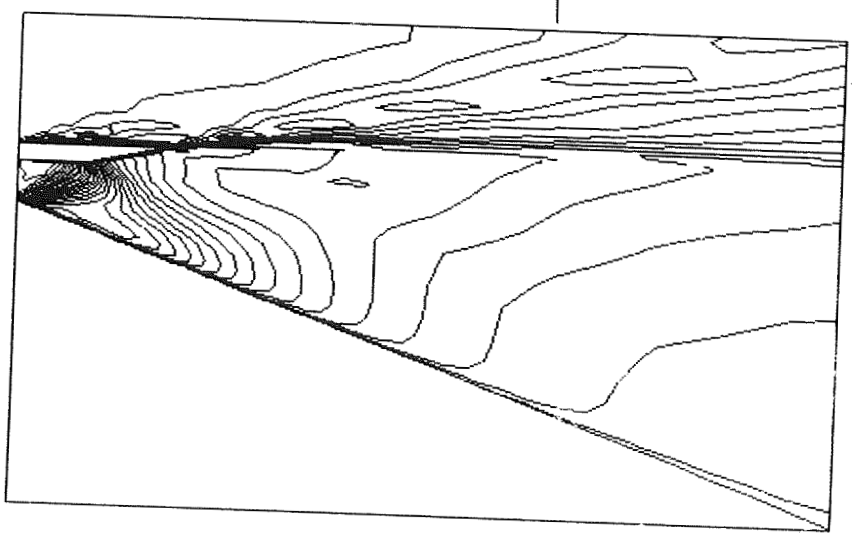

Fig. 17 Density Contours, Side View
l=11

a. j=14

b. j=28

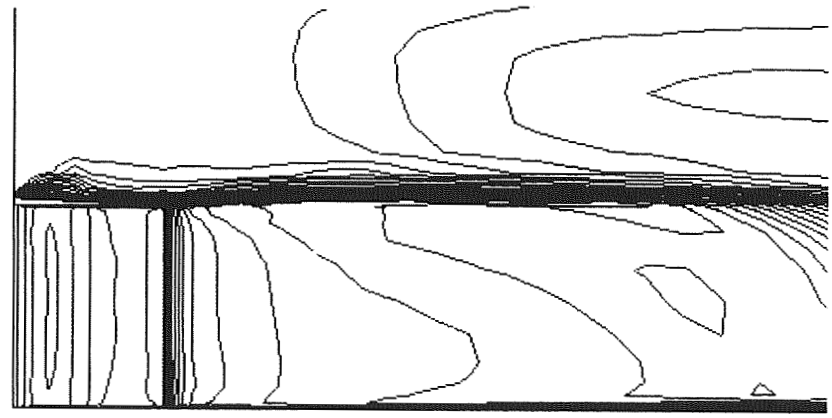

Fig. 18 Mach Number Contours, Top Views

c. j=43

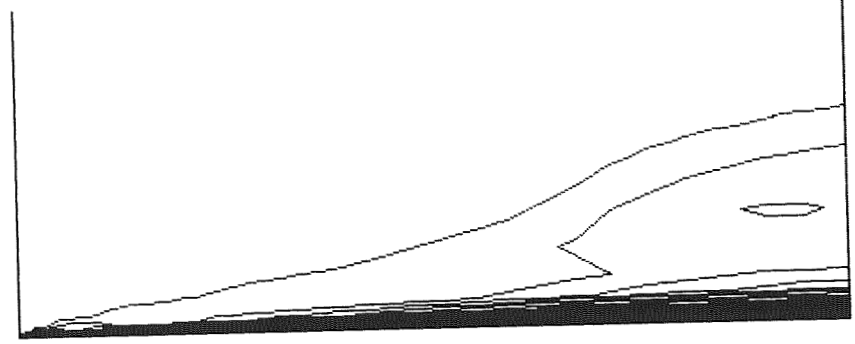

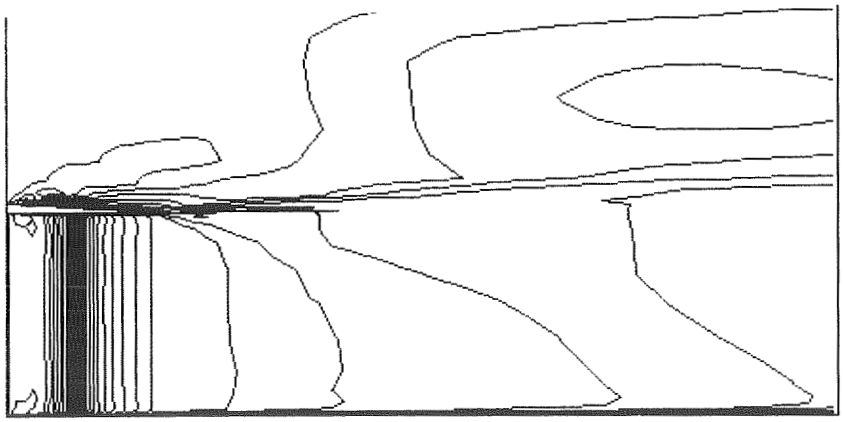

Fig. 19 Density Contours, Top View
j=25

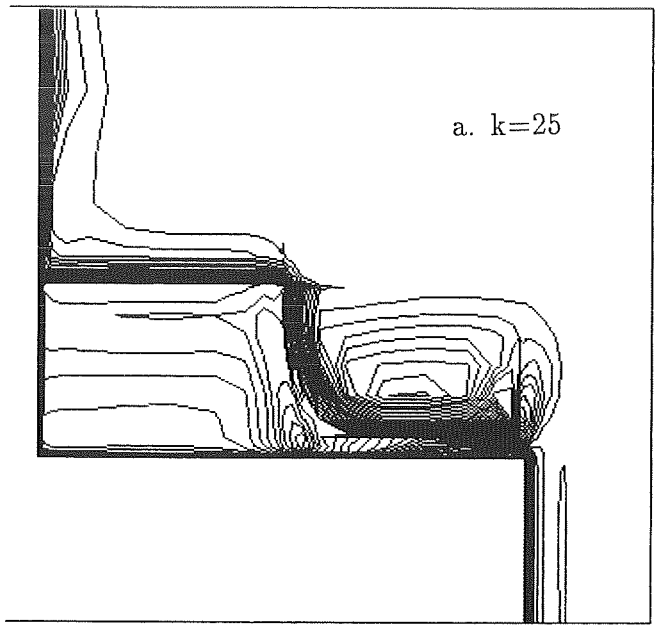

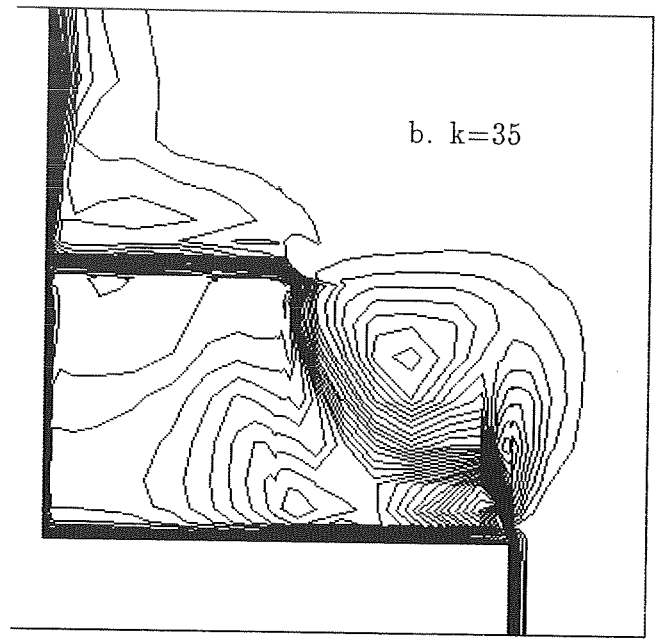

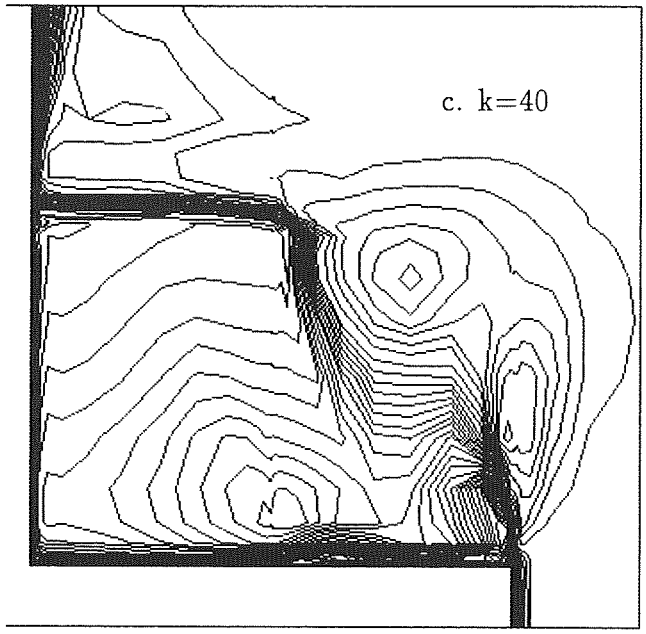

Fig. 20 Mach Number Contours, Rear Views

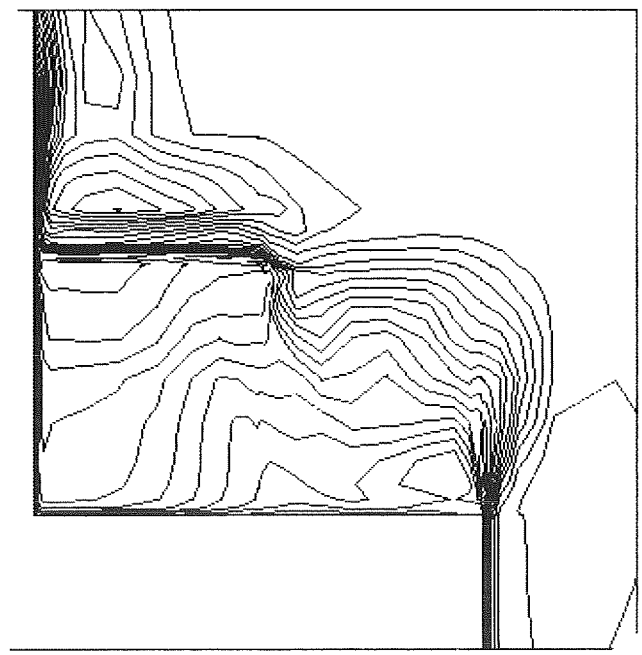

Fig. 21 Density Contours, Rear View
k=35

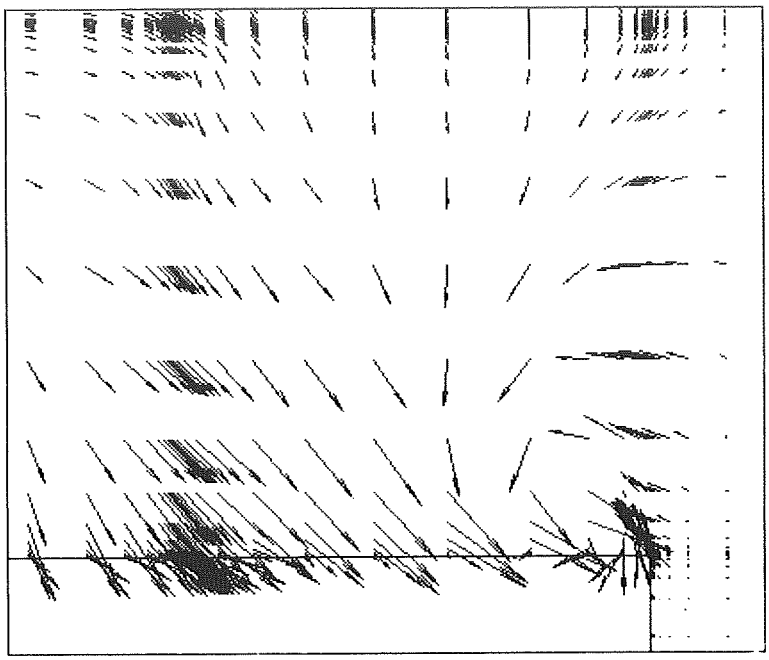

Fig. 22 Spanwise Total Velocities, i=35

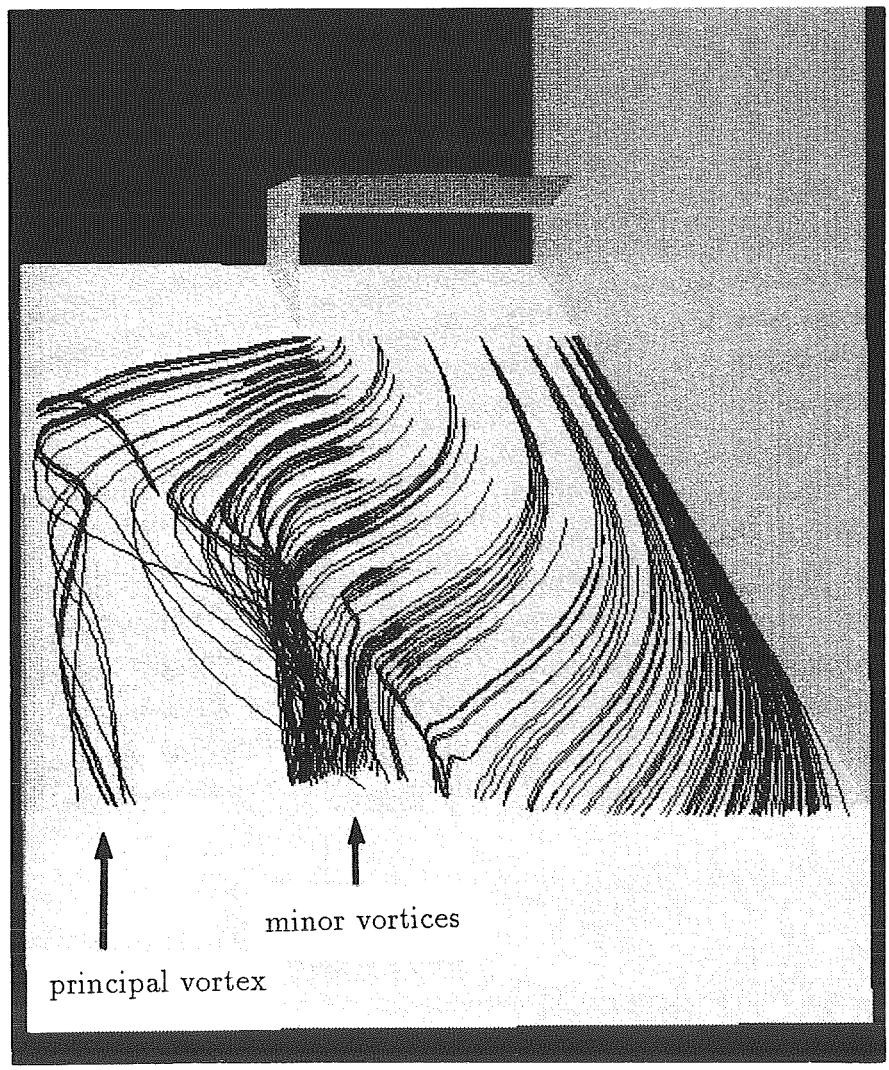

Fig. 23 Particle Trajectories

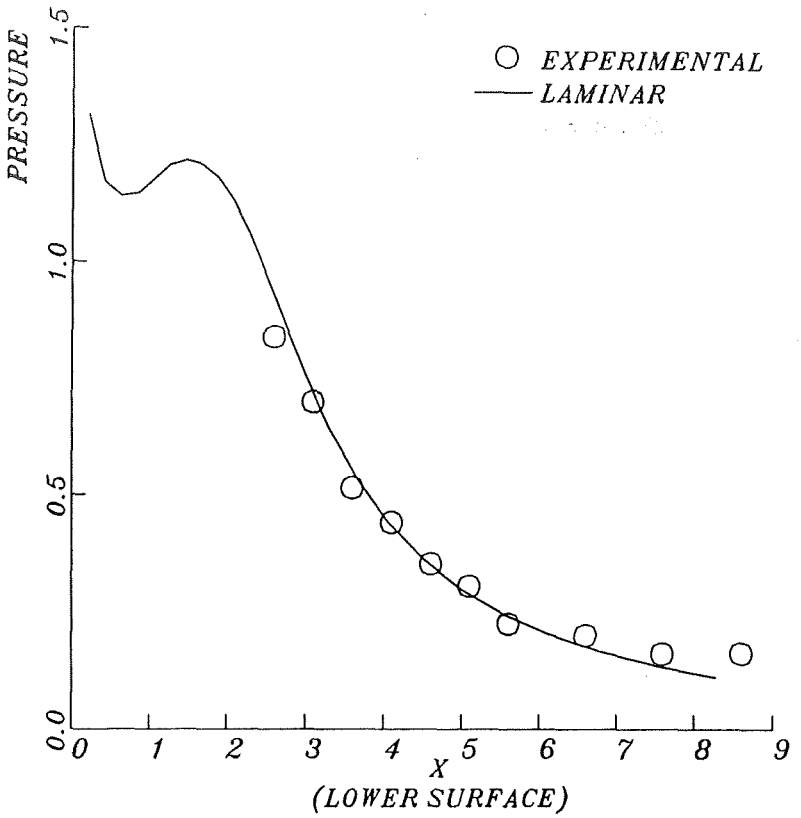

a. z=0.75, near the Reflection Plate

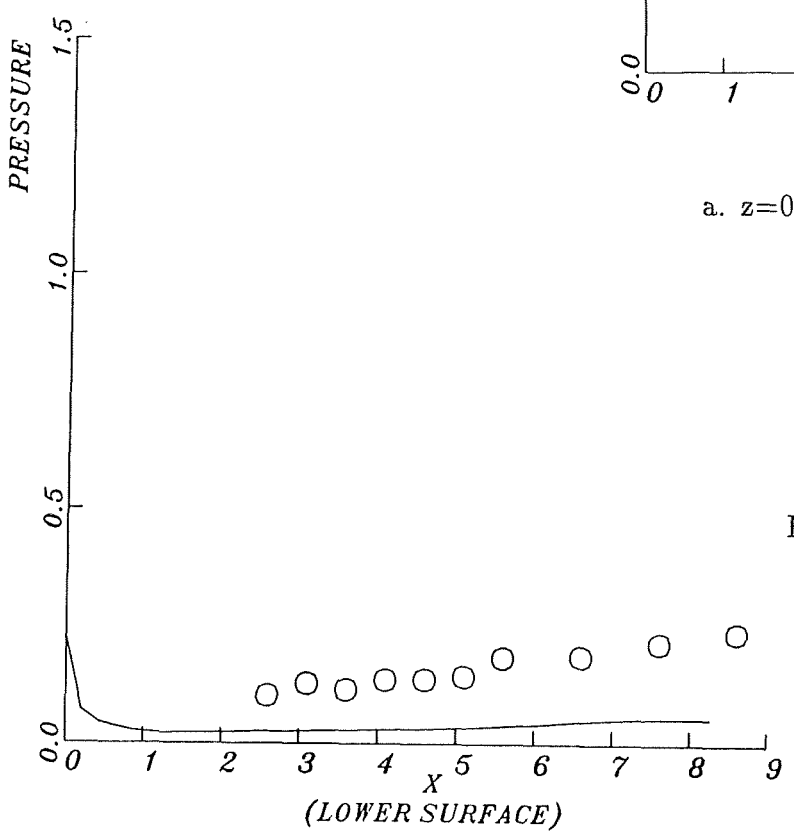

b. z=4.52, near the Short Sidewall

Fig. 24 Wall Pressure Distributions